Astron. Astrophys. 337, 85–95 (1998)

ASTRONOMY AND ASTROPHYSICS

# Two-dimensional radiative transfer with transiently heated particles: methods and applications

**V. Manske and Th. Henning**

Astrophysical Institute & University Observatory Jena, Schillergäßchen 3, D-07745 Jena, Germany
(manske@astro.uni-jena.de, henning@astro.uni-jena.de)

Received 22 December 1997 / Accepted 27 May 1998

**Abstract.** We present a combined treatment of two-dimensional (2D) continuum radiative transfer together with the emission of transiently heated small dust grains. To calculate this emission, an efficient and numerically stable algorithm was developed, which is outlined in detail. Using this new radiative transfer code, we were able to model the infrared emission of the starburst galaxy NGC 6090. We found that the assumed presence of transiently heated particles inside the dust torus of NGC 6090 is in agreement with the observed data. Special attention is given to the PAH emission lines, discovered in recent ISOPHOT-S observations of NGC 6090.

Our results show clearly that the emission of small particles influences significantly spectral energy distributions and intensity maps. Especially at wavelengths shorter than 10 $\mu$m, transiently heated particles are the main source of infrared radiation. Therefore, transiently heated particles seem to be highly relevant for understanding the nature of objects were these particles are present.

**Key words:** radiative transfer – dust,extinction – ISM: molecules – galaxies: active – galaxies: starburst – infrared: galaxies

## 1. Introduction

In the mid-fifties Platt (1955) investigated the optical properties of tiny interstellar dust grains ($\mathrm{radii} \approx 10$ Å). Almost two decades later Greenberg & Hong (1974) and Purcell (1976) showed that such small grains undergo temperature fluctuations in the interstellar environment. Andriesse (1977) proposed these temperature fluctuation to be the reason for the observed near- and mid- ($0.8\mu\mathrm{m} \leq \lambda \leq 20\mu\mathrm{m}$) infrared excess observed in M17. Since then, temperature fluctuations of small grains were made responsible for the near- and mid- infrared excess in various other kinds of objects, i.e. in planetary nebulae (Sellgren 1984), diffuse HI regions and dark clouds (Draine & Anderson 1985), and in the circumstellar environment of Herbig Ae/Be stars (Natta et al. 1993, Natta & Krügel 1995).

Furthermore, it turned out that many astrophysical objects show infrared emission lines in their spectral energy distributions. Since their discovery by Gillett et al. (1973) these "unidentified" IR features were found in many different classes of objects. They include planetary nebulae, emission and reflection nebulae (Geballe et al. 1985, Cohen et al. 1986, Russell et al. 1977, Bregman et al. 1989), proto-planetary nebulae (Buss et al. 1990), the environment of Be and Herbig Ae/Be stars (Tokunaga et al. 1991, Schutte et al. 1990, Brooke et al. 1993), active galactic nuclei (Gillett et al. 1975, Willner et al. 1977, Acosta-Pulido et al. 1996), and the general interstellar medium (Giard et al. 1988a,b, Mattila et al. 1996). Léger & Puget (1984) and Allamandola et al. (1989) proposed the IR features to be emission lines of polycyclic aromatic hydrocarbons (PAHs). This hypothesis was recently strengthened by discovering PAH molecules by probing carbonaceous chondrites (Clemett & Messenger 1996).

Up to now, many authors reported methods to calculate the emission from small particles (radii $< 100$ Å), i.e. Greenberg & Hong (1974), Purcell (1976), Draine & Anderson (1985), Dwek (1986), Léger et al. (1989), and Guhathakurta & Draine (1989). But only little progress was made in considering temperature fluctuations of small particles in radiative transfer calculations. In fact, many radiative transfer codes were developed to handle spherically symmetric (Yorke 1979, Rowan-Robinson 1980), axisymmetric (Efstathiou & Rowan-Robinson 1990, Spagna et al. 1991, Pier & Krolik 1992, Granato & Danese 1994, Sonnhalter et al. 1995, Men'shchikov & Henning 1997) or, in principle, arbitrarily shaped dusty envelope configurations (Yorke 1986, Stenholm 1995). However, all these codes consider only thermal emission of "classical" grains. As calculating the emission of small grains is much more time-consuming, temperature fluctuations were taken into account only for spherically symmetric dust clouds (Lis & Leung 1991, Siebenmorgen et al. 1992, Szczerba et al. 1997). However, the availability of an approximate, but very efficient 2D radiative transfer code (Men'shchikov & Henning 1997, Manske et al. 1997) enabled us, for the first time, to include a treatment of temperature fluctuations of small dust grains in 2D radiative transfer calculations.

In Sect. 2, we describe in detail a numerically stable and efficient algorithm to calculate the emission of small dust particles. In Sect. 3, the radiative transfer code is described as well as the implementation of the emission from small grains. In Sect. 4, we apply our code to the starburst galaxy NGC 6090 to show the effect of temperature fluctuations on spectral energy distri-

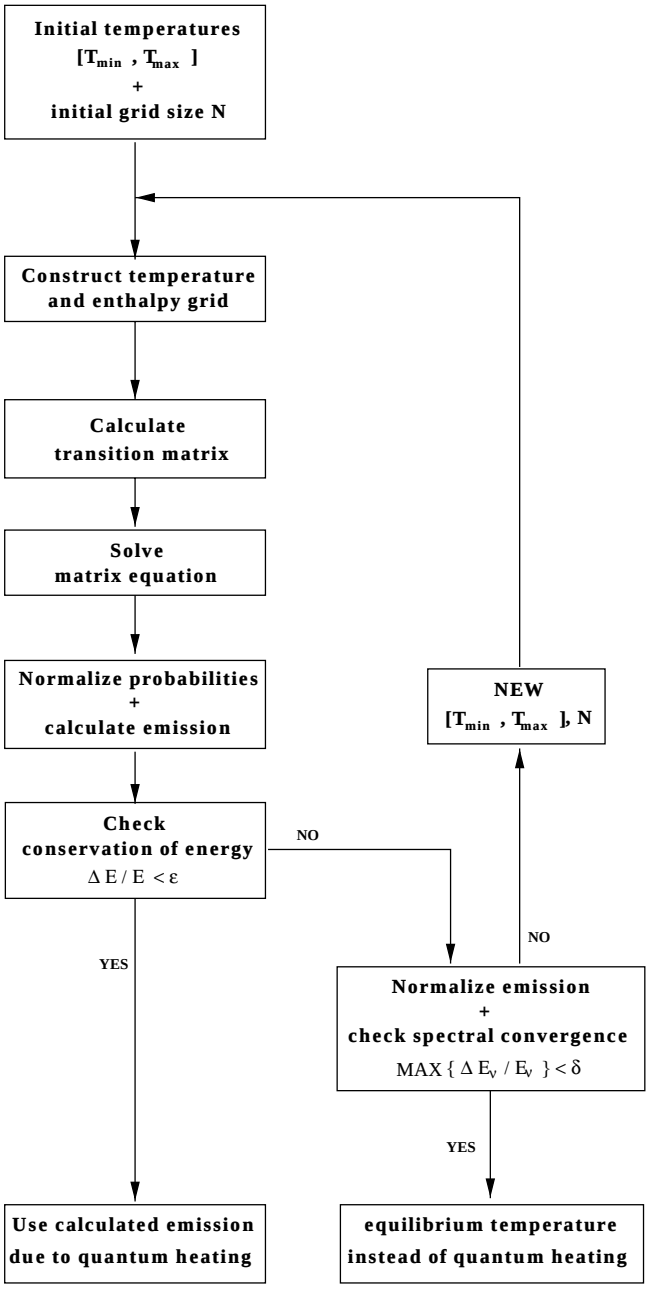


**Fig. 1.** Algorithm used to calculate the emission of small dust grains due to quantum heating.

butions and intensity maps. We finish the paper in Sect. 5 with the conclusions.

## 2. Quantum heating

Standard interstellar dust grains (radii $>$ 100 Å ) are large enough to be in thermal equilibrium with an outer radiation field. Therefore, an equilibrium temperature $(T_{\rm eq})$ can be obtained using the balance equation

$$\int_0^\infty \sigma(\nu)^{\rm abs}\, J_\nu \,{\rm d}\nu = \int_0^\infty \sigma(\nu)^{\rm abs}\, B_\nu(T_{\rm eq})\,{\rm d}\nu\,, \qquad (1)$$

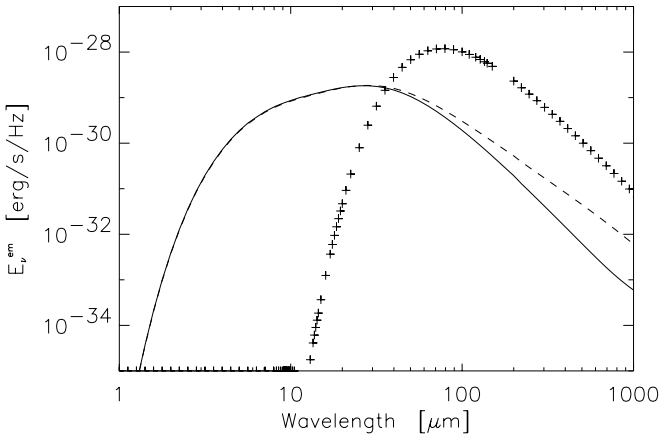


**Fig. 2.** Emission of a 10 Å graphite grain located at a distance of 1pc from a B-type star ($L_\star = 10^4 L_\odot$, $T_\star = 2 \cdot 10^4$K). The solid line represents the emission calculated using the complete cooling equation ( Eq. (4)) and the dashed line is emission for approximative cooling after Eq. (5). The "+" signs indicate the "classical" emission after Eq. (1), which is shown to illustrate the effect of quantum heating. Note that for both kinds of matrix definitions the frequency-integrated emission is the same.

where $J_\nu$ is the mean intensity of the incoming radiation field at the frequency $\nu$, $B_\nu$ the Planck function, $\sigma(\nu)^{\rm abs}$ the absorption cross section, and $T_{\rm eq}$ the temperature of the dust grain.

The heat capacity of smaller dust grains, however, is so low that even the absorption of one UV/visible photon can increase the heat content of the grain substantially. As a result of this, small dust grains undergo temperature fluctuations if they are exposed to UV radiation. Therefore, instead of an equilibrium temperature, a temperature distribution is required. In this paper, we will refer to this effect, which is often called *transient heating*, as to *quantum heating* because the effect is related to the absorption of individual photons.

Two methods published in previous papers for calculating the quantum heating process seem to be applicable for radiative transfer calculations. The first one we refer to (Sect. 2.1) is a general method for calculating the quantum heating process of small particles and was developed by Guhathakurta & Draine (1989). The second one (Sect. 2.2) was mainly developed by Léger et al. 1989 to calculate the emission of PAHs, and was first used in radiative transfer calculations by Siebenmorgen & Krügel (1992).

### *2.1. Emission of small dust grains*

To calculate the emission of small dust grains (radii $<$ 100 Å), we use an extension of the method developed by Guhathakurta & Draine (1989), hereafter GD89. Knowing the range of the temperature fluctuations $[T_{\rm min}, T_{\rm max}]$, a grid for temperatures $T_i$ and corresponding enthalpies $U_i$ is created. For these (artificial) energy levels, transition rates per unit time $(A_{f,i})$ for heating $(f > i)$ and cooling $(f < i)$ can be calculated. After solving the stationary matrix equation for the probabili-

ties $P_i$ of finding the grain in the $i-$th bin (in the temperature interval $[T_i - \frac{T_i - T_{i-1}}{2}, T_i + \frac{T_{i+1} - T_i}{2}]$),

$$\frac{\mathrm{d}P_f}{\mathrm{d}t} = \sum_{i=1}^{N} A_{f,i}\, P_i = 0\ ,\ f = 1, ..., N \quad ;\ \sum_{i=1}^{N} P_i = 1 \tag{2}$$

the monochromatic energy per unit time $E_\nu^{em}$ emitted by the grain can be obtained by

$$E_\nu^{em} = 4\pi\sigma(\nu)^{abs} \sum_{i=1}^{N} B_\nu(T_i)\, P_i\,, \tag{3}$$

In the following section we present details on calculating the transition matrix and solving Eq. (2) as well as some results for carbon grains.

This method, starting from the definition of the temperature grid up to the calculation of the emitted intensity, is implemented as the inner loop in the algorithm summarized in Fig. 1.

### 2.1.1. Transition matrix

Following the formalism of GD89, the matrix elements for cooling from state $i$ to state $f$ are defined by

$$A_{f,i} = -\frac{4\pi}{\Delta U_i} \int\limits_{\nu_{f,i}-\Delta\nu_f/2}^{\nu_{f,i}+\Delta\nu_f/2} \sigma(\nu)^{\mathrm{abs}} B_\nu(T_i)\, \mathrm{d}\nu\,, \tag{4}$$

where $U_i$ and $\Delta U_i$ are the values and widths of the enthalpy bins. The frequencies $\nu_{f,i}$ and $\Delta\nu_f$ are defined by $\nu_{f,i} = (U_i - U_f)/h$ and $\Delta\nu_f = \Delta U_f/h$.

To solve Eq. (2) for the complete matrix (cooling according to Eq.(4)), we used the bi-conjugate gradient method BiCGStab of Sleijpen & Van der Vorst (1995), where the solution of the approximate matrix (cooling after Eq. (5)) is used for preconditioning. Due to the nature of the matrix, standard matrix solvers like LU-decomposition or the Gauß algorithm (Press et al. 1986) failed to give reliable results.

Because solving Eq. (2) for such a matrix can be very time-consuming, GD89 used a more simple approach to calculate the cooling rates. In their approximation, cooling from level $i$ occurs only to the next lower level $f = i-1$. Therefore, cooling rates are given by,

$$A_{f,i} = \begin{cases} -\frac{4\pi}{\Delta U_i} \int\limits_0^\infty \sigma(\nu)^{\mathrm{abs}} B_\nu(T_i)\, \mathrm{d}\nu & : \quad f = i-1 \\ 0 & : \quad f = 1, ..., i-2 \end{cases} \tag{5}$$

A matrix defined in such a way is a lower triangular matrix with only one additional upper side diagonal and, therefore, Eq. (2) can now be solved directly, what makes the procedure very fast. There is no physical reason for this approximative treatment of cooling because the temperature and enthalpy levels are artificial, whereas the physical states are expected to form a quasi-continuum.

This procedure can only be understood in terms of numerics. If "coarse" grids are used, the widths of the enthalpy bins often increase to such an extent that the integration limits numerically approach $[0, \infty]$ in Eq. (4). This effectively transforms Eq. (4) into Eq. (5).

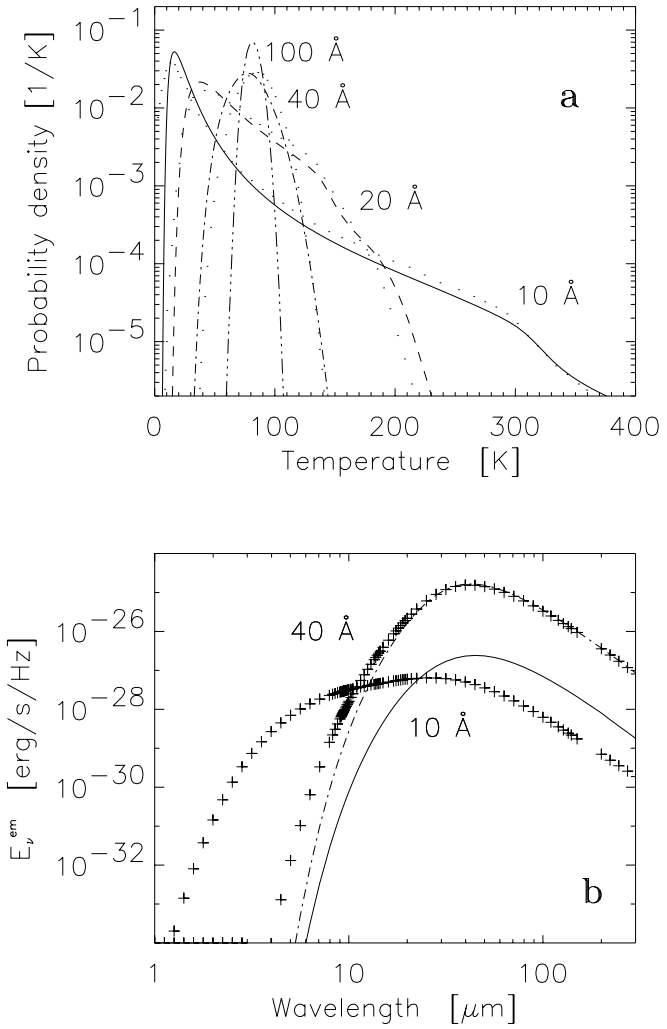


**Fig. 3. a** Probability densities for graphite grains (after Eq. 5) located at a distance of $5 \cdot 10^{17}$cm from a B-type star ($L_\star = 10^4 L_\odot$, $T_\star = 2 \cdot 10^4$K). The dots represent the results of Siebenmorgen et al. (1992). **b** Emission of 10 and 40 Å graphite grains due to quantum heating. The "+" signs indicates the emission obtained when assuming thermal equilibrium.

In Fig. 2, we show the emission of a 10 Å graphite grain located in the vicinity of a B-type star, and obtained by the use of both kinds of transition matrices. For wavelengths up to 30 $\mu$m both methods produce almost identical emission. However, in case of longer wavelengths, using cooling according to Eq. (5) systematically underestimates the emission up to an order of magnitude. These differences are due to the larger number of transition channels which are available if the exact cooling (Eq. (4)) is used.

To test our implementation of the quantum heating algorithm, we compared our results with those published by Siebenmorgen et al. (1992). To illustrate the effect of quantum heating, the emission of the 10 and 40 Å grains are compared with

the emission obtained under the assumption of thermal equilibrium (Eq. (1)). In Fig 3a, one can nicely see the effect of grain size on the probability density. The probability density broadens with decreasing grain size. In the "classical limit" where the grain reaches thermal equilibrium, the distribution becomes almost a $\delta$-function. In Fig. 3b, the main effect of quantum heating, namely the increase of emission shortwards of about $10\mu$m wavelength, is clearly observable. For the environment used here, $40$Å sized grains are almost in thermal equilibrium. As one can see from Fig. 3a, the resulting probability densities are quite similar to the densities obtained by Siebenmorgen et al. (1992).

### 2.1.2. Adaptive temperature grid

For the calculations shown in Fig. 3, we used a fixed temperature grid. But as illustrated in Fig. 4a–f, the probability distribution is not calculated with sufficient accuracy if the grid is too coarse. Not only the shape of the probability distribution may be wrong, also its maximum may be located at the wrong position. A good indicator for the reliability of the solution of Eq. (2) is the conservation of energy. As shown in Table 1, the quantity $\Delta E_{\rm rel}$ decreases with increasing number of temperature grid points. Here, the deviation from the conservation of energy $\Delta E_{\rm rel}$ and the absorbed and emitted energies per unit time are defined by

$$\begin{aligned} \Delta E_{\rm rel} &= ABS\left(E_{\rm abs} - E_{\rm em}\right)/E_{\rm abs} \\ E_{\rm abs} &= 4\pi \int_0^\infty \sigma(\nu)^{\rm abs} J_\nu \,{\rm d}\nu \\ E_{\rm em} &= 4\pi \int_0^\infty \sigma(\nu)^{\rm abs} \sum_{i=1}^{N} B_\nu(T_i)\, P_i \,{\rm d}\nu \,. \end{aligned} \tag{6}$$

To calculate the transition matrix and to solve Eq. (2) may take several seconds on a DEC-Alpha 3000/500 workstations if more than 200 grid points are used. Depending on the size of the dust particle and on the spectral energy distribution of the outer radiation field, much more grid points may be required to obtain reliable results (Table 1).

If the quantum heating of small grains is considered in 2D radiative transfer calculations it is necessary to apply the procedure described above up to several thousand times during one run of the code. Therefore, even gaining only one second CPU time for each quantum heating calculation results in a significant acceleration of the combined code. From this point of view, it does not seem to be appropriate to use always several hundreds of grid points to ensure reliable results for the quantum heating calculations. Hence, we developed the algorithm shown in Fig. 1.

The basic idea of this algorithm is to calculate the quantum heating via an iterative scheme. For each iteration, a new temperature interval $[T_{\rm min}, T_{\rm max}]^{\rm new}$ is chosen, based on an analysis of the probability densities obtained from the previous iteration. The new interval excludes temperatures which are not necessary for the quantum heating calculation (adaptive temperature grid) and is defined by

$$[T_{\rm min}, T_{\rm max}]^{\rm new} =$$

**Table 1.** Conservation of energy due to quantum heating calculation for the plots presented in Fig. 4a–f

| 40 Å grain | | | | |
|---|---|---|---|---|
| Bins | 50 | 100 | 200 | 400 |
| $\Delta E_{\rm rel}$ | 26.0 | 3.7 | 0.75 | 0.15 |
| **40 Å grain (with iterations)** | | | | |
| Iteration | 1 | 3 | 5 | 6 |
| Bins | 50 | 112 | 252 | 387 |
| $T_{\rm min}, T_{\rm max}$ | 300, 1100 | 417, 793 | 444, 756 | 453, 755 |
| $\Delta E_{\rm rel}$ | 28 | .48 | .18 | .08 |
| **10 Å grain** | | | | |
| Bins | 50 | 100 | 200 | |
| $\Delta E_{\rm rel}$ | below 10 % | | | |

$$\left\{T \,\epsilon\, [T_{\rm min}, T_{\rm max}]^{\rm old} \;\mid\; P(T)/P_{\rm max} > 10^{-14}\right\}\,, \tag{7}$$

where $P_{\rm max} = MAX_i\left\{P_i\right\}$. Additionally, to further increase the accuracy of the calculations, the number of temperature grid points is increased by 50% for every new iteration.

We found that another good indicator to check the convergence of the quantum heating algorithm, apart from the conservation of energy, is the maximum spectral deviation $\Delta E_{\rm spec}^{\rm max}$ defined by

$$\Delta E_{\rm spec}^{\rm max} = MAX_{\{\nu\}}\left\{{\rm ABS}\left(B_\nu(T_{\rm eq}) - J_\nu^{\rm em}\right)/B_\nu(T_{\rm eq})\right\}, \tag{8}$$

where the emitted mean intensity $J_\nu^{\rm em}$, which is defined by

$$J_\nu^{em} = \sum_{i=1}^{N} B_\nu(T_i)\, P_i\,, \tag{9}$$

was multiplied by the factor $E_{\rm abs}/E_{\rm em}$ to correct for remaining numerically-caused deviations from conservation of energy. Apart from indicating convergence of the algorithm, $\Delta E_{\rm spec}^{\rm max}$ provides information about the importance of the quantum heating for the analyzed grain (under the actual radiative conditions). A small spectral deviation indicates that quantum heating can be neglected for all larger grains exposed to the same radiation field. Their emission can be calculated using Eq. (1) whereas high levels of spectral deviation, like those shown in Fig. 4a–f f, are clear indicators for the necessity of using the quantum heating algorithm.

In the current implementation of the algorithm (Fig. 1), we use $\epsilon = 10^{-1}$ (limit for $\Delta E_{\rm rel}$) and $\delta = 10^{-2}$ (limit for $\Delta E_{\rm spec}^{\rm max}$). We also tested our code by using smaller values for $\epsilon$ and $\delta$ but this did not significantly influence the results. The deviations around $1\mu$m in the cases shown in Fig. 4a–f d-f, together with the criteria we just introduced, demonstrate that quantum heating has to be taken into account for these grain sizes.

The effect of iterating can be seen by comparing the results of Fig. 4a–fa with those of Fig. 4a–fb. Already with an adapted 252-point grid, the position and shape of the probability density curve are similar to those obtained by a 400-point grid without

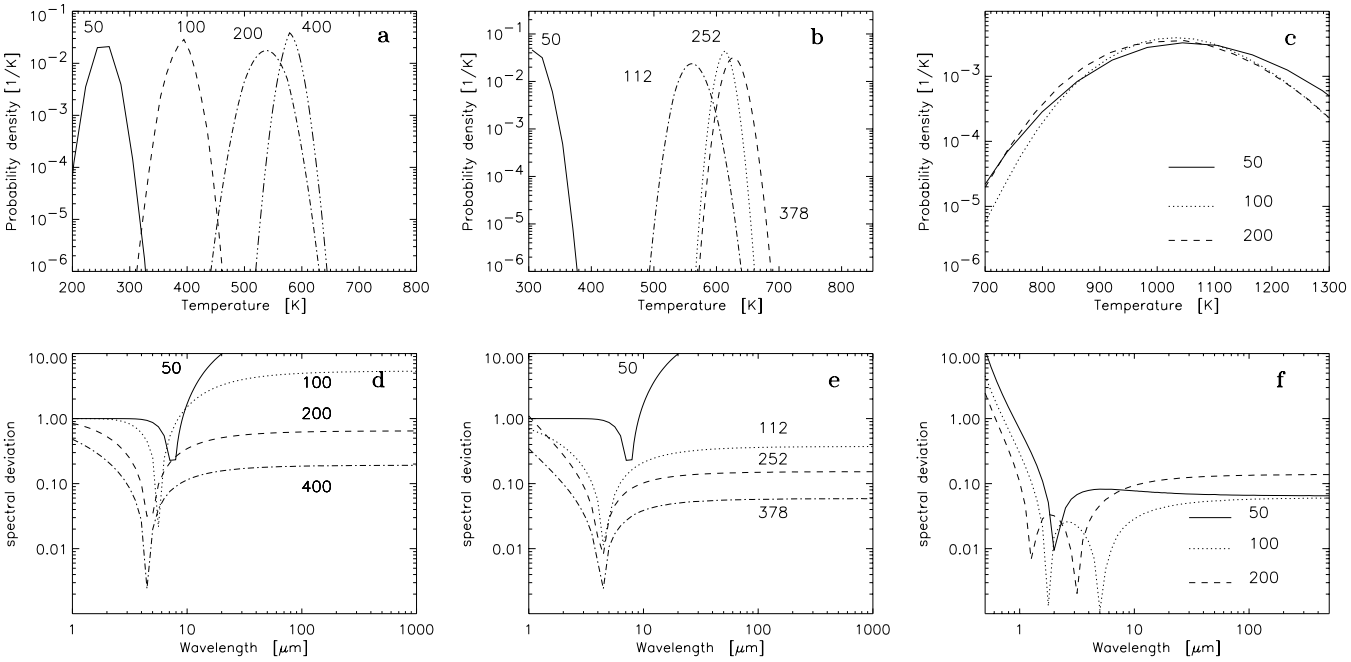


**Fig. 4a–f.** Probability densities and spectral deviation $\Delta E_{\rm spec}(\nu) = \mathrm{ABS}\left(B_\nu(T_{\rm eq}) - J_\nu^{\rm em}\right)/B_\nu(T_{\rm eq})$ for 40 and 10 Å graphite grains near a B-type star ($L_\star = 10^4 L_\odot$, $T_\star = 2 \cdot 10^4$K). Left row: results for a 40 Å grain at $5 \cdot 10^{15}$cm distance using a fixed temperature interval of $[T_{\rm min}, T_{max}] = [300, 1100]$ K and different numbers of grid points. Middle row: like the left row but using the iterative scheme from Fig. 1 with adaptive temperature grids, see Table 1 for details on temperature grids. Right row: results for a 10 Å grain at $10^{15}$cm distance using a fixed temperature interval of $[T_{\rm min}, T_{max}] = [4, 3000]$ K. The equilibrium temperatures (after Eq. (1)) are 605 K for the 40 Å grain, and 1084 K for the 10 Å grain.

iterating (for energy conservation, see Table 1). Additionally, with the 252-point grid (Fig. 4a–fe), almost the same low levels in spectral deviation are reached as for the 400-point grid without iterating (Fig. 4a–fd). For the sake of comparison, the resulting probability density and spectral deviation for a 10 Å grain located in the same environment as the 40 Å grain are presented in Fig. 4a–fc,f. Here, the results are much less sensitive to the number of temperature grid points for a simple reason. For a given temperature grid, the width of the enthalpy bins is proportional to the number of atoms in the grain. Therefore, they are proportional to the cube of the grain radius. This results in a much finer enthalpy grid if the grain size decreases.

Our calculations clearly show that the use of fixed temperature grids, even if they contain about 400 grid points, cannot always ensure reliable results for the quantum heating of small interstellar dust grains. We demonstrated that iterative schemes with adaptive grids are a good approach to obtain a sufficient and controlled accuracy, for all grain sizes and environments of astrophysical interest. Using the algorithms presented above (Fig. 1), enables us to consider the emission from small grains in a 2D radiative transfer code.

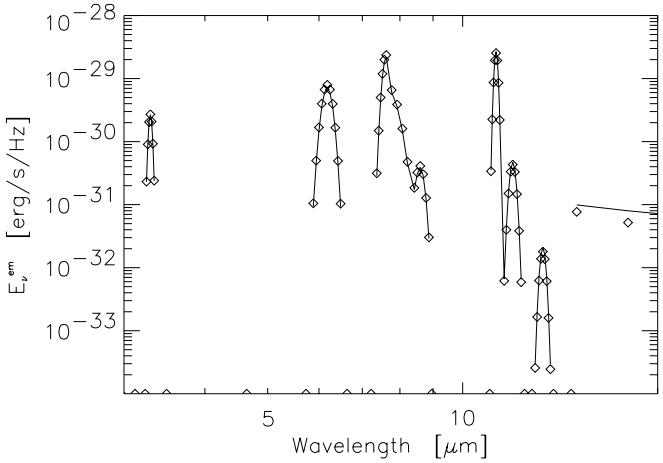


**Fig. 5.** Emission of a compact PAH consisting of 30 carbon atoms, located at a distance of $5 \cdot 10^{17}$cm from a B-type star ($L_\star = 10^4 L_\odot$, $T_\star = 2 \cdot 10^4$K). The solid line is for the emission calculated using the method of GD89, whereas the diamonds indicate the results obtained using the cooling curve (Eq. (11)). The absorption cross section of the PAH was taken from Schutte et al. (1993).

### *2.2. Heating of PAHs*

In general, we use the same quantum heating algorithm for the PAHs as for the small dust grains, assuming that the absorption cross section of PAHs is independent of temperature. But as PAHs may consist of only some dozens of carbon atoms, the time between the absorption of two UV/visible photons (Eq. (10)) can be so long that the PAH can cool down via IR emission, before the next high-energy photon impinges. In this case, a much faster method is used to calculate the emission, based on

the results of Léger et al. (1989). It was first used in radiative transfer calculations (for spherical geometry) by Siebenmorgen et al. (1992):

First, the mean time $t_{\rm UV}$ for absorbing a UV/visible photon is determined,

$$\frac{1}{t_{\rm UV}} = 4\pi \int_0^{\nu_{\rm cut}} \frac{\sigma(\nu)^{\rm abs}\, J_\nu}{h\nu}\, {\rm d}\nu\,, \tag{10}$$

where $\nu_{\rm cut}$ denotes the low-frequency cut-off in the UV/visible absorption cross section of the PAHs. Knowing the energy absorbed during this time interval, the peak temperature and corresponding enthalpy $E_{\rm peak}$ can be calculated. Then, the PAH cools down via IR-emission, according to the energy-time dependence found by Allamandola et al. (1989), and Léger et al. (1989)

$$E(t) = [E_{\rm peak}^{-0.4} - 0.004t]^{-2.5}\,,\ \text{energies in } cm^{-1}\,. \tag{11}$$

Here we assume that this cooling behaviour found for chrysene (24 C-atoms) is also valid for all larger compact PAHs. For each time step $i = 1, ..., N$ during the cooling (Eq. ( 12)) conservation of energy is considered,

$$\int_0^{\nu_{\rm cut}} \sigma(\nu)^{\rm abs}\, J_\nu\, {\rm d}\nu$$
$$= \int_0^{\infty} \sigma(\nu)^{\rm abs}\, B_\nu(T(t_i))\, {\rm d}\nu - \frac{\Delta E(t_i)}{4\pi\, \Delta t_i} \tag{12}$$

with $\Delta E(t_i) = E(t_{i-1}) - E(t_i)$ and $\Delta t_i = t_i - t_{i-1}$. Finally, the emission is again obtained by a superposition of blackbody curves, similar to Eq. (3), with probabilities $\tilde{P}_i$ given by

$$\tilde{P}_i = \frac{\int_0^{\nu_{\rm cut}} \sigma(\nu)^{\rm abs}\, J_\nu\, {\rm d}\nu + \frac{\Delta E(t_i)}{4\pi\, \Delta t_i}}{\int_0^{\infty} \sigma(\nu)^{\rm abs}\, B_\nu(T(t_i))\, {\rm d}\nu}\,, \sum_0^N \tilde{P}_i = 1\,. \tag{13}$$

In Fig. 5 we compare the emission for a PAH obtained using both kinds of calculation methods, the matrix method of GD89 (Eqs. (2) - (5)) and the cooling curve method (Eqs. (10) - (13)).

We conclude in agreement with Siebenmorgen et al. (1992) that the cooling curve method gives reliable results for large absorption times $t_{\rm UV}$. Actually, we demand that $t_{\rm UV} > 5$ minutes, which is much larger than the typical "cooling time scale" of about 10 seconds (Allamandola et al. 1989).

## 3. The radiative transfer code

For the calculation of the continuum radiative transfer in 1D (spherical symmetry) and 2D (flared disk geometry) dust configurations, we used the code developed by Manske et al. (1997) which is based on the method given by Men'shchikov & Henning (1997). The main approximation used in this code is that even for the disk geometry, the density depends on the radial coordinate only. In addition, mean intensities and temperatures

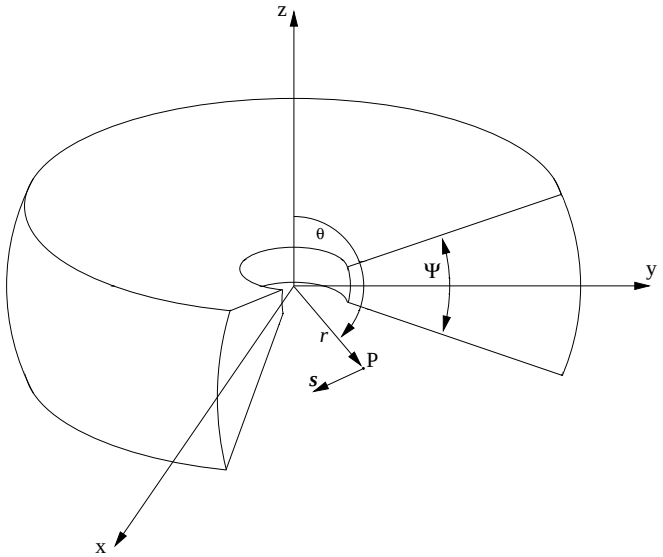


**Fig. 6.** Geometry of the model disk with the opening angle $\Psi$

are self-consistently calculated for points in the disk's midplane and at its upper and lower conical surfaces only. The disk itself is essentially a part of a sphere with two removed polar cones (Fig. 6). A more detailed descriptions of the strategy for the solution of the radiative transfer problem can be found in our earlier papers mentioned above.

### *3.1. Implementation of quantum heating*

In the code, a ray tracing technique is used to solve the radiative transfer equation. This means that this equation is reduced to a 1-dimensional equation (Eq. (14)), which has to be solved along rays $\boldsymbol{s}$, with corresponding impact parameters $p$.

$$\mu \frac{{\rm d}I_\nu(r,\mu)}{{\rm d}s} = -\kappa^{\rm ext}(\nu)\ [I_\nu - S_\nu] \tag{14}$$

Here $r$ is the radial position, $\boldsymbol{s}$ is the direction of the ray, and $\mu = \pm\sqrt{1 - p^2/r^2}$. Assuming isotropic scattering and that the grains are in thermal equilibrium, the source function is defined by

$$S_\nu = \frac{1}{\kappa(\nu)^{\rm ext}} \sum_{i,k} \left[\kappa(\nu)_{i,k}^{\rm abs}\, B_\nu(T_{i,k}) + \kappa(\nu)_{i,k}^{\rm sca}\, J_\nu\right], \tag{15}$$

where $J_\nu$ is the mean intensity, $B_\nu$ is the Planck function and $T_{i,k}$ is the temperature of the dust grains of the chemically distinct dust component $i$ and the size bin $k$. The quantities $\kappa(\nu)_{i,k}^{\rm abs}$ and $\kappa(\nu)_{i,k}^{\rm sca}$ are the absorption and scattering coefficients of the dust component $(i,k)$, and $\kappa(\nu)^{\rm ext}$ is the total extinction coefficient, defined by:

$$\kappa(\nu)^{\rm ext} = \sum_{i,k} \left[\kappa(\nu)_{i,k}^{\rm abs} + \kappa(\nu)_{i,k}^{\rm sca}\right]\ . \tag{16}$$

If the dust model contains small dust grains, so that the quantum heating method must be used to calculate the emission, the

source function has to be modified in order to account for this effect:

$$S_\nu = \frac{1}{\kappa(\nu)^{\rm ext}} \sum_{i,k}^{\rm big} \kappa(\nu)^{\rm abs}_{i,k} B_\nu(T_{i,k}) + \frac{1}{\kappa(\nu)^{\rm ext}} \sum_{i,k}^{\rm small} \kappa(\nu)^{\rm abs}_{i,k} \sum_j B_\nu(T_{i,k,j}) P_j + \frac{1}{\kappa(\nu)^{\rm ext}} \sum_{i,k} \kappa(\nu)^{\rm sca}_{i,k} J_\nu \, . \quad (17)$$

Here "small" means grains with radii $< 100$ Å and $P_j$ denotes the probabilities obtained by the quantum heating algorithm from Fig. 1.

To illustrate the difficulties of considering quantum heated particles in radiative transfer codes, note that it may take up to 25 seconds CPU time (on a DEC-Alpha 3000/500 workstation) to apply the quantum heating algorithm (Fig. 1) for **one** grain species and at **one** spatial grid point for **one** iteration. However, due to the basic approximations in our radiative transfer code, the numerical effort in flared disk geometry is only twice as high as for spherical symmetry (1D codes). For the models presented in this paper, the typical CPU time on a DEC-Alpha 3000/500 was about 6 hours.

## 4. Application: the starburst galaxy NGC 6090

The starburst galaxy NGC 6090 is located at a distance of about 117 Mpc ($\rm H_0 = 75 km s^{-1} Mpc^{-1}$). Observations in the optical by Mazzarella & Boroson (1993) show that NGC 6090 is an interacting pair of galaxies in the process of being merged. The two nuclei are separated by a distance of $\approx 3600$pc and have comparable luminosities. First ISO results, recently reported by Acosta-Pulido et al. (1996), show strong PAH emission lines. Therefore, any modeling of NGC 6090 has to take into account emission from quantum heated particles.

### *4.1. Energy sources*

To model NGC 6090 we used an association of OB-type stars ($T_\star = 3 \cdot 10^4$K) in combination with red-giant stars ($T_\star = 3 \cdot 10^3$K). Both kinds of stars are assumed to have the same total luminosity of $6.5 \cdot 10^{10} L_\odot$, which results in a total luminosity of $L_{\rm source} = 1.3 \cdot 10^{11} L_\odot$ for the central source. The source itself is surrounded by a molecular dusty torus. To account for starbursts, additional radiative sources ("starburst sources") located inside the dust torus were added. These "starburst sources" are treated in a similar way as the so-called "hot spots" of Krügel & Siebenmorgen (1994):
Each of the "starburst sources" consists of a B-star ($L_\star = 3 \cdot 10^3 L_\odot$, $T_\star = 2 \cdot 10^4$K) surrounded by a homogeneous, optically thin dust envelope ($\tau_{550\rm nm} = 0.5$). For the sake of computational simplicity, the "starburst sources" are assumed to form distinct concentric shells of starburst activity inside the dust torus. For our best-fit model (Fig. 7), we used 27 shells of starburst activity. Each of them has a luminosity of $L_{\rm burst} = 10^9 L_\odot$. They are located each at 20 pc distance starting at a distance of 10 pc from the central source. However, the exact positions of the starburst sources have only very little effect on the results of the radiative transfer calculations.

### *4.2. The dusty torus*

#### 4.2.1. Dust models

In a detailed modeling, one might have to use dust mixtures consisting of amorphous carbon and silicate grains as well as grains with ice mantles (Men'shchikov & Henning 1997). These should correspond to the physical conditions in the objects which are studied, e.g., dense molecular cloud cores (Ossenkopf & Henning 1994, Preibisch et al. 1993, Henning et al. 1995), protostellar envelopes (Lenzuni et al. 1995) or protoplanetary accretion disks (Henning & Stognienko 1996). For silicates, recent optical data measured for cosmic dust analogues (Jäger et al. 1994, Dorschner et al. 1995) are available.

Applying Mie theory, we calculated the coefficients of absorption and scattering for compact spherical grains.

The power-law index $q$ of the grain size distribution

$$n(a) \propto a^{-q} \ , a_{\rm min} \le a \le a_{\rm max} \quad (18)$$

is set to 4.

The dust used in this work is composed of silicate, graphite, and amorphous carbon grains with the optical data from Dorschner et al. (1995), Draine (1985), and Preibisch et al. (1993), respectively, as well as of PAHs. According to chemical composition and heating mechanism, we have six distinct dust components:

1. Big silicate grains with radii between 0.05 $\mu$m and 1$\mu$m.
2. Big graphite grains (0.05 $\mu$m to 1$\mu$m).
3. Big amorphous carbon grains (0.05 $\mu$m to 1$\mu$m).
4. Small silicate grains (0.001 $\mu$m (10 Å) to 0.01 $\mu$m (100 Å))
5. Small graphite grains (0.001 $\mu$m (10 Å) to 0.01 $\mu$m (100 Å))
6. Compact PAH molecules, composed of 30 to 500 carbon atoms, with the absorption cross sections from Schutte et al. (1993).

The silicate to carbon mass-ratio is 1:2 and the mass ratio of graphite to amorpous carbon is 2:1. To simplify matters, we have chosen the same sublimation temperature of 1500 K for all dust grains, whereas the PAHs may exist up to temperatures of 2500 K.

To calculate the quantum heating of the small silicate and graphite grains, the internal energy of the grains as a function of temperature is required. In agreement with GD89, for the graphite particles we used the analytic fit to the graphite enthalpy data of Chase et al. (1985).

$$E(T) = \frac{4.15 \cdot 10^{-22} T^{3.3}}{1 + 6.52 \cdot 10^{-3} T + 1.5 \cdot 10^{-6} T^2 + 8.3 \cdot 10^{-7} T^{2.3}}, \quad (19)$$

where E(T) is in erg per atom. These enthalpies were also used for the PAHs. Léger et al. (1989) pointed out that the specific heat of PAHs is comparable to the one of carbon, especially if the PAHs are in a dehydrogenated state.

For the silicate grains we used a fit to experimental results for $SiO_2$ and obsidian (Léger et al. 1985).

$$C(T) = \begin{cases} 1.4 \cdot 10^3 \ T^2 & : \quad T \leq 50\mathrm{K} \\ 2.2 \cdot 10^4 \ T^{1.3} & : \quad 50 \leq T \leq 150\mathrm{K} \\ 4.8 \cdot 10^5 \ T^{0.68} & : \quad 150 \leq T \leq 500\mathrm{K} \\ 3.41 \cdot 10^7 & : \quad T \geq 500\mathrm{K}, \end{cases} \tag{20}$$

where $C(T)$ is the specific heat in erg per $\mathrm{cm}^{-3}$ per K, which is related to the enthalpy by

$$E(T) = \int_0^T C(\tilde{T})\,\mathrm{d}\tilde{T}\,. \tag{21}$$

To account for the fact that the enthalpies described above were determined for bulk material, whereas we apply them to clusters of N atoms, the enthalpies had to be multiplied by a correction factor of $1 - \frac{2}{N}$.

According to the grain size distribution, for the dust model containing big and small dust grains, the ratio of masses of small dust grains $M_{\mathrm{small}}$ to big grains $M_{\mathrm{big}}$ is $M_{\mathrm{small}} : M_{\mathrm{big}} = 1 : 1$. The amount of PAHs is assumed to be 3% of the mass of the total carbon content of the dust torus, being fairly in agreement with estimates by Pendleton et al. (1994). To reduce the strength of the C-H lines we choose a degree of dehydrogenation of 90%.

#### 4.2.2. The model torus

The dust torus used to model NGC 6090 is assumed to have a radius of 900 pc and an opening angle of $\Psi = 170°$. The observations of Mazzarella & Boroson (1993) indicate that NGC 6090 is viewed almost face-on. Therefore, the line of sight was chosen to have a viewing angle of $80°$ above the torus midplane. The value for the opening angle of the torus is somewhat constrained by the required optical depth (see below).

The density distribution used for the model torus is given by

$$\rho(r) \propto \begin{cases} r^0 & : \quad R_{\mathrm{min}} \leq r \leq 0.1 \cdot R_{\mathrm{max}} \\ r^{-1} & : \quad 0.2 \cdot R_{\mathrm{max}} < r \leq R_{\mathrm{max}} \end{cases}. \tag{22}$$

The dust mass is $M_{\mathrm{dust}} = 6.75 \cdot 10^6 M_\odot$ resulting in an optical depth along the line of sight, in direction to the central source, of $\tau_{550\mathrm{nm}} = 40$. For this value of optical depth the strength of the silicate absorption feature ($\lambda = 10\mu$m) obtained from the model matches the observed data (Fig. 7).

### *4.3. Results*

As shown in Fig. 7, even this simple model gives a reasonable fit to the ISOPHOT-data. It reproduces the main spectral characteristics of NGC 6090. The calculated spectral energy distribution (SED) fits well to the observed 10 $\mu$m silicate absorption feature and produces similar fluxes at longer wavelengths. The somewhat plateau-like structure around 15 $\mu$m is also reproduced. On the other hand, the model SED shows too few emission in the far infrared region ($\lambda > 100\,\mu$m). But the far-infrared emission can be explained by emission from cool (23 K) dust located outside the nuclei of NGC 6090. This emission from the host galaxy is included in the observed data but not covered by our torus model. In Fig. 8, we compare our results with the ISOPHOT-SL data obtained by Acosta-Pulido et al. (1996). ISOPHOT-SS data were not taken into account because according to Acosta-Pulido et al. (1996) theses data are too noisy to be used in a detailed analysis. All calculated PAH line intensities are roughly in agreement with the observed ones. However, the line-widths are somewhat different. Additionally, the observed 6 $\mu$m, 7.6 $\mu$m, and 11 $\mu$m feature seem to have slightly different center-wavelengths as the corresponding features in our model but this is mainly red-shift caused ($z = 0.03$). However, a more

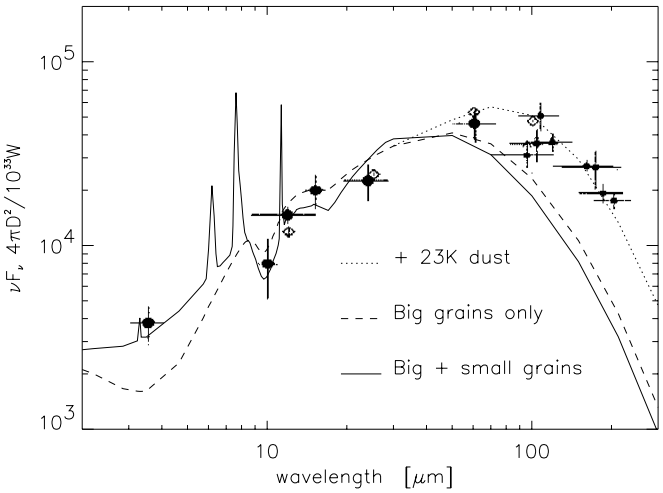


**Fig. 7.** Best fit model SED for NGC 6090, illustrating the effect of quantum heating. The numerical results are compared to IRAS and recent ISO data (Acosta-Pulido et al. 1996). Filled circles: ISOPHOT-P aperture measurements, filled squares ISOPHOT-C measurements, open diamonds: IRAS values. The fluxes obtained from our models are multiplied by a factor of two, to account for the bi-nuclear structure of NGC 6090.

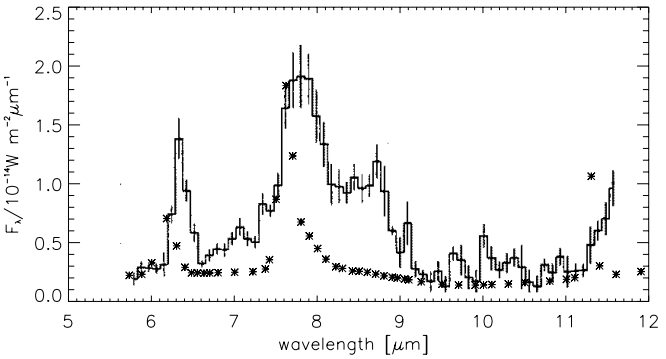


**Fig. 8.** Comparison of observed and calculated PAH emission. The astrisks represents the fluxes from our model SED, the vertical bars are the ISOPHOT-SL data published by Acosta-Pulido et al. (1996).

detailed fit of the SED of NGC 6090 seems not desirable, at the moment: First, even for the most recent ISOPHOT observations (Acosta-Pulido et al. 1996) the area covered at the distance of NGC 6090 is much larger than 2000 pc in radius (torus diameter), especially at wavelengths larger than 10 $\mu$m. Therefore, the emission at infrared wavelengths is systematically somewhat underestimated by the model. However, Acosta-Pulido et al. (1996) pointed out that the observed emission at wavelengths above 100 $\mu$m can be explained by emission from diffuse interstellar dust. Second, a detailed fit of the observed PAH emission lines is extremely challenging because of the many free parameters which are necessary to parameterize the dust model: size limits for the small grains, mass ratio of small to big grains, grain size power law exponent, sizes of the PAHs, degree of ionisation and hydrogenation of PAHs. Especially the ionisation and dehydrogenation of PAHs have significant influence on line widths and relative line intensities. Moreover, astrophysical PAH models contain mainly compact PAHs (i.e. Léger et al. 1989, Schutte et al. 1993), whereas also non-compact PAHs may be present in space. Each of these parameters, or even all together, may be responsible for the differences between the observed and calculated PAH emission fluxes. However, a detailed fit of the infrared lines is not the basic intention of this paper. The PAH model is basically used to demonstrate the capabilities of the new combined radiative transfer code. Further investigations may show that other materials, i.e. very small hydrogenated amorphous carbon (HAC) grains, are necessary to explain some aspects of the observed infrared features. As soon as the specific heat data of these materials are available, their emission can be calculated with the code developed by us.

#### 4.3.1. Effect of quantum heating

Apart from the appearance of the PAH emission lines, the main effect of including quantum heated particles on the SEDs can be nicely seen in Fig. 7. It is the increase of emission at wavelengths shortwards of 10 $\mu$m, balanced by the decrease of emission in the FIR ($\lambda \geq 20\mu$m).

Not only the total emission is affected by quantum heating, it also changes the temperature structure of the dust torus and, therefore, the intensity maps. In Fig. 9 we present intensity maps for our best-fit torus model for both kinds of dust models. Due to the orientation of the dust torus relative to the line of sight, the horizontal (east-west direction in observations) intensity profiles are symmetrical with respect to their center. In the vertical (north-south direction) intensity profiles the asymmetry of the projection of the torus surface onto the plane of sky can be seen. Here, the majority of intensity asymmetry originates from dust around the polar cones of the torus.

As already indicated by the SED (Fig. 7), the flux in the FIR is dominated by emission of big dust grains. For $\lambda = 100\mu$m the intensity maps show comparable levels of emission at most points in the torus, whether quantum heated particles are present or not. The higher total emission seen in Fig. 7 originates from higher intensities at the inner torus points. At shorter wavelengths, the picture changes. In the inner hot parts of the torus, where most of the UV radiation emitted by the central source is converted to the IR, the emission of small quantum heated grains is, in general, higher than those of the big grains. This results in the somewhat plateau-like structures seen in the maps for $\lambda = 30$, 18, and 7.6 $\mu$m. In the outer cooler parts of the torus, where the thermal emission of dust peaks at wavelengths above

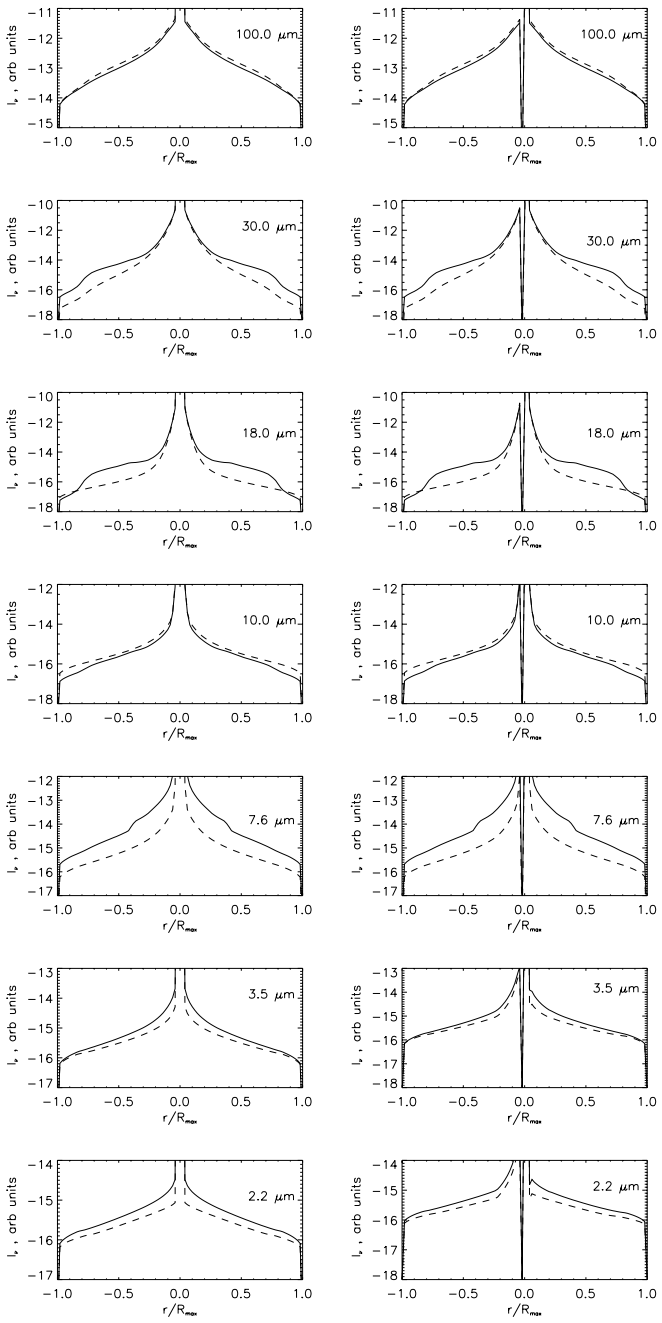


**Fig. 9.** Horizontal (left column) and vertical (right column) intensity profiles of the model torus for various wavelengths. In each panel we compare the results obtained for the dust model containing quantum heated particles (full line) with those obtained using the dust model consisting only of big grains (dashed line). The abscissa is always in fractions of the torus radius. The ordinates show logarithms of intensities in arbitrary units.

10 $\mu$m ($T_{\rm dust} \approx 300$ K and lower), the quantum heating "shifts" emission to shorter wavelengths. This effect can be seen by the inspection of the maps for 10 $\mu$m. In the inner regions (about 10 % of the torus radius) the emission from big grains is comparable to the emission from dust including small particles. But as the distance to the central source increases, the emission from big grains dominates more and more. Moreover, the maps for 2, 3.3, and 7.6 $\mu$m illustrate that at shorter wavelengths quantum heating is the dominant source of dust emission, all over the dust torus. For $\lambda = 3.3$ and $7.6\mu$m this effect is strengthened by the fact that PAH emission lines are located at these wavelengths. Hence, the PAH emission increases the continuum emission of big grains up to an order of magnitude, independently of their location in the dust torus.

## 5. Conclusion

We described an efficient and numerically stable algorithm, based on the results of Guhathakurta & Draine (1989) and Léger et al. (1989), to calculate the quantum heating of small dust grains and of PAHs. The iterative procedure, combined with adaptive temperature grids and quality checks (conservation of energy, spectral deviation) leads to reliable results for all kinds of grain sizes and radiation fields. We demonstrated the need for such algorithms to calculate quantum heating at a reliable accuracy, especially if quantum heating should be used in radiative transfer calculations, in the presence of grain size distributions, and for various types of local radiation fields.

For the first time, a quantum heating algorithm is included in a 2D radiative transfer code. This new code enabled us to model the IR emission of the starburst galaxy NGC 6090. Our calculations proved that quantum heated small particles influence significantly the SED as well as the intensity maps of the dust torus. It even happens that continuum emission of small grains is the dominant source of dust radiation at most NIR to MIR wavelengths, for all points inside the dust torus. Naturally, this effect is much stronger for the emission lines of the PAHs.

Despite the fact that it may be possible to fit the continuum emission using dust composed only of big grains, the results obtained this way would lead to a completely wrong interpretation of the observations, because completely different density and temperature distributions would be derived. Therefore, we conclude that any modeling concerning dusty objects which show PAH lines must include quantum heating if reliable interpretations of the data are the goal.

## References


Acosta-Pulido J.A., Klaas U., Laureijs R.J., et al., 1996, A&A 315, L121

Allamandola L.J., Tielens A.G.G.M., Barker J.R., 1989, ApJS 71, 733

Andriesse C.D., 1977, A&A 66, 169

Bregman J. D., Allamandola, L. J., Witteborn, F. C., Tielens, A. G. G. M., Geballe, T. R.,1989, ApJ 344, 791

Brooke T.Y., Tokunaga A.T., Strom S.E., 1993, AJ 106, 656

Buss R.H.Jr., Cohen M., Tielens A.G.G.M., et al., ApJ 365, L23

Chase M.W. Jr., Davies C.A., Downey J.R.Jr., et al., 1985, Phys.Chem.Ref.Data 14, Suppl. No. 1

Cohen M., Allamandola L.J., Tielens A.G.G.M., et al., 1986, ApJ 302, 737

Clemett S.J., Messenger S., Chillier X.D.F., et al., 1996, Lunar and Planetary Science 27, 229

Dorschner J., Begemann B., Henning Th., Jäger C., Mutschke H., 1995, A&A 300, 503

Draine B.T, 1985, ApJS, 57, 587

Draine B.T., Anderson N., 1985, ApJ 292, 494

Dwek E., 1986, ApJ 302, 363

Efstathiou A., Rowan-Robinson M., 1990, MNRAS 245, 275

Geballe T.R., Lacy J.H., Persson S.E., McGregor P.J., Soifer B.T., 1985, ApJ 292, 500

Giard M., Serra G., Caux E., Pajot F., Lamarre J. M., 1988a, A&A 201, L1

Giard M., Serra G., Caux E., Pajot F., Lamarre J. M., 1988b, A&A 215, 92

Gillett F.C., Forrest W.J., Merrill K.M., 1973, ApJ 183, 87

Gillett F.C., Kleinmann D.E., Wright E.L., Capps R.W., 1975, ApJ 198, L65

Granato G.L., Danese L., 1994, MNRAS 268, 235

Greenberg J.M., Hong S.S., 1974, in *IAU Symposium 60, Galactic and Radio Astronomy*, eds. F. Kerr and S.C. Simon III, Reidel, Dordrecht, p. 155

Guhathakurta P., Draine B.T., 1989, ApJ 345, 230

Henning Th., Stognienko R., 1996, A&A 311, 291

Henning Th., Michel B., Stognienko R., 1995, PS&SS 43, 1333

Jäger C., Mutschke H., Begemann B., Dorschner J., Henning Th., 1994, A&A 292, 641

Krügel E., Siebenmorgen R., 1994, A&A 282, 407

Léger A., Puget J.L., 1984, A&A 137, L5

Léger A., Jura M., Omont A., 1985, Astr. Ap., 144, 147

Léger A., d'Hendecourt L., Défourneau D., 1989, A&A 216, 148

Lenzuni P., Gail H.P., Henning Th., 1995, ApJ 447, 848

Lis D.C., Leung C.M., 1991, Icarus 91,7

Manske V., Henning Th., Men'shchikov A.B., 1997, A&A in press

Mathis J.S., Rumpl W., Nordsieck K.H., 1977, ApJ 215, 425

Mattila K., Lemke D., Haikala L.K., et al., 1996, A&A 315, 353

Mazzarella J.M, Boroson T.A., 1993, ApJS 85, 27

Men'shchikov A.B., Henning Th., 1997, A&A, 318, 879

Natta A., Prusti T., Krügel E, 1993, A&A 275, 533

Natta A., Krügel E, 1995, A&A 302, 849

Ossenkopf V., Henning Th., 1994, A&A 291, 943

Pendleton Y.J., Sandford S.A., Allamandola L.J., Tielens A.G.G.M., Sellgren K., 1994, ApJ 437,, 683

Pier E.A., Krolik J.H., 1992, ApJ 401, 99

Platt J.R., 1955, ApJ 123, 486

Press W.H., Teukolsky S.A., Vetterling W.T., Flannery B.P., 1986, *Numerical Recipes*, Cambridge University Press, Cambridge, Chap. 2

Preibisch Th., Ossenkopf V., Yorke H., Henning Th., 1993, A&A 279, 577

Purcell E.M., 1976, ApJ 206, 685

Rowan-Robinson M., 1980, ApJS 44, 403

Russell R.W., Soifer B.T., Merrill K.M., 1977, ApJ 213, 66

Schutte W.A., Tielens A.G.G.M., Allamandola L.J., Cohen M., Wooden D.H., 1990, ApJ 360, 577

Schutte W.A., Tielens A.G.G., Allamandola L.J., 1993, ApJ 415, 397

Sellgren K., 1984, ApJ 277, 623

Siebenmorgen R., Krügel E., 1992, A&A 259, 614

Siebenmorgen R., Krügel E., Mathis J.S., 1992, A&A 266, 501
Sleijpen G.L.G., Van der Vorst H.A., 1995, Appl. Numer. Math., 19, 235
Sonnhalter C., Preibisch Th., Yorke H.W., 1995, A&A 299, 545
Spagna G.F., Leung C.M., Egan M.P., 1991, ApJ 379, 2325
Stenholm L., 1995, A&A 290, 393
Szczerba R., Omont A., Volk K., Cox P., Kwok S., 1997, A&A 317, 859
Tokunaga A.T., Sellgren K., Smith R.G., et al., 1991, ApJ 380, 452
Willner S.P., Soifer B.T., Russell R.W., Joyce R.R., Gillett F.C., 1977, ApJ 217, L121
Yorke H.W., 1979, A&A 86, 286
Yorke H.W., 1986, in *Astrophysical Radiation Hydrodynamics*, eds. K. Winkler & M.L. Norman, Reidel, Dordrecht, p 141